Enhancing π-Delocalization and Suppressing Traps via Doping in Electron Transport Materials for Efficient Semitransparent Organic Photovoltaics

Yating Mo[1], Jiayu Wang[1] ✉, Hanjiao Chen[2], Yufei Gong[3], Jianglong Zhou[4], Junhao Lu[1], Cenqi Yan[1], Lei Meng[3], Liang-Wen Feng[4], Yongfang Li[3], Pei Cheng[1] ✉

HIGHLIGHTS

- High-performance semitransparent organic photovoltaics (STOPVs) with decreased electrical loss were fabricated via introducing lithium bis(trifluoromethanesulfonyl)imide (LiTFSI) to electron transport layer (ETL).

- LiTFSI interacts with ETL material PDINN and enhanced π-delocalization in PDINN, which is beneficial to conductivity and thereby electron collection range.

- LiTFSI-doped PDINN-based STOPVs show an improved power conversion efficiency of 14.3%, average visible transmittance of 29.0%, and light utilization energy of 4.15%, which is among the highest values of optical structure-free STOPVs.

ABSTRACT The ultrathin metal electrode in semitransparent organic photovoltaics (STOPVs) usually suffers from limited charge collection capability and conductivity and thus hinders the power conversion efficiency (PCE). Herein, a new strategy of enhancing the π-delocalization of electron transport layer (ETL) via lithium bis(trifluoromethanesulfonyl)imide doping is developed. The enhanced π-delocalization in ETL benefits sizeable intermolecular π–π overlap, prone to harvesting electrons and thereby improving charge collection range. Doping also improves the conductivity of both ETL and ultrathin silver electrode. Furthermore, the trap densities in ETL and STOPV devices are reduced after doping, contributing to suppressed

recombination and higher PCE. Consequently, ETL doping maintains an average visible transmittance of ~ 30% while promotes the PCE of STOPVs from 13.0% to 14.3% and light utilization efficiency from 3.74% to 4.15%, which is among the highest values of optical structure-free STOPVs. This work provides a new insight of π-delocalization manipulation in ETL for efficient STOPVs.

KEYWORDS Semitransparent organic photovoltaics; Interfacial engineering; π-delocalization; Surface traps; Electrical loss
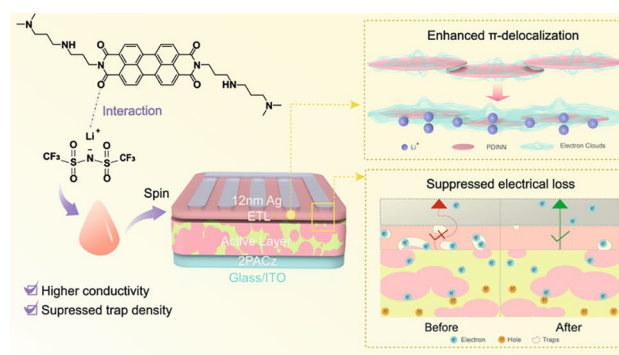
✉ Jiayu Wang, wangjiayu@scu.edu.cn; Pei Cheng, chengpei@scu.edu.cn

[1] College of Polymer Science and Engineering, State Key Laboratory of Advanced Polymer Materials, Sichuan University, 610065 Chengdu, People's Republic of China

[2] Analytic & Testing Center, Sichuan University, 610065 Chengdu, People's Republic of China

[3] Beijing National Laboratory for Molecular Sciences, CAS Key Laboratory of Organic Solids, Institute of Chemistry, Chinese Academy of Sciences, 100190 Beijing, People's Republic of China

[4] Key Laboratory of Green Chemistry & Technology, Ministry of Education, College of Chemistry, Sichuan University, 610065 Chengdu, People's Republic of China

1 Introduction

Semitransparent organic photovoltaics (STOPVs) leverage the discontinuous absorption properties of organic semiconductors, enabling them to possess both light transmittance and electricity generation capabilities [1–5]. Given their potential applications in a variety of settings, such as agricultural greenhouses [6, 7], smart windows [8, 9], and floating photovoltaics [10], STOPVs have gained escalating interest. The average visible transmittance (AVT) and power conversion efficiency (PCE) are two vital parameters for assessing the performance of STOPVs. The optimal PCE of opaque organic photovoltaics (OPVs) has surpassed 20% in recent years owing to molecular [11–15] and device engineering [16–20], while those of the highest-performing STOPVs with an AVT of approximately 30% still lag behind with significantly decreased short-circuit current density (J_{SC}) [21–24]. To achieve high PCE at a given AVT, lots of effective strategies have been reported to maximize the light harvesting in near-infrared region to compensate the optical loss in visible region, such as designing new active layer materials and incorporating third components [25–32].

However, the current loss in STOPVs is not solely attributed to optical loss, and electrical loss is another significant factor responsible for performance degradation [3, 33]. The electrical loss continuously increases as the Ag electrode thickness is reduced from 100 to 10 nm, accompanied by a dramatic rise in surface trap density by three orders of magnitude [34]. Therefore, reducing surface traps and unnecessary electrical loss in STOPVs is of great importance for enhancing their photovoltaic performance. Lots of works have demonstrated that the thickness of transparent Ag electrodes is insufficient to form an efficient conductive network, although thin Ag electrodes exhibit considerable transparency and fabrication simplicity [35–37]. Near the threshold thickness, Ag typically exhibits limited charge collection range, suboptimal lateral conductivity, and increased defects, which dominate the electrical loss in STOPVs [37–39]. Interfacial engineering strategies, such as introducing seed layer [40] or covalent interaction [33], were reported to ameliorate the performance of thin Ag. To further improve the performance of STOPVs, diverse and effective approaches need to be explored. Recently, a longitudinal through-hole architecture was reported to eliminate the dependence on ultrathin metal electrode. In STOPVs with this architecture, opaque silver grid is used as top electrode and responsible for efficient charge collection, while the longitudinal holes through the device contribute to optical transparency, achieving PCEs of 6–15% with AVT of 60–10% [41].

Herein, we proposed a new strategy of enhancing the electron collection ability and conductivity of ultrathin metal electrode via electron transport layer (ETL) doping (Scheme 1). Lithium bis(trifluoromethanesulfonyl) imide (LiTFSI), consisted of strong electron-withdrawing $TFSI^-$ anions and a Li^+ cation, is used as the dopant. LiTFSI interacts with ETL material PDINN through electrostatic interaction between Li^+ and carbonyl group and induces a more delocalized π electron distribution in PDINN, which is beneficial to intermolecular π–π overlap and thereby electron collection range. After LiTFSI doping, the PDINN ETL exhibits improved conductivity from 9.67×10^{-5} to 1.71×10^{-4} S cm^{-1}, increased doping density from 2.69×10^{16} to 4.01×10^{16} cm^{-3}, and reduced trap density from 1.29×10^{17} to 7.26×10^{16} cm^{-3}. Charge dynamic analysis further demonstrates that LiTFSI-doped PDINN (D-PDINN)-based STOPVs present enhanced charge extraction, suppressed charge recombination and inhibited surface traps relative to PDINN-based counterparts. As a result, compared with PDINN-based STOPVs with a PCE of 13.0%, an AVT of 28.8% and a light utilization efficiency (LUE = PCE × AVT) of 3.74%, D-PDINN-based STOPVs show an improved PCE of 14.3%, a comparable AVT of 29.0% and a higher LUE of 4.15%, which is among the highest values of optical structure-free STOPVs.

2 Experimental Section

2.1 Materials

2PACz, PM6, BTP-eC9, and PDINN were purchased from Hyper Materials. LiTFSI was purchased from Alladin Materials. PEDOT:PSS 4083 was purchased from Heraeus. PDINO and PDNIT-F3N were purchased from Solarmer.
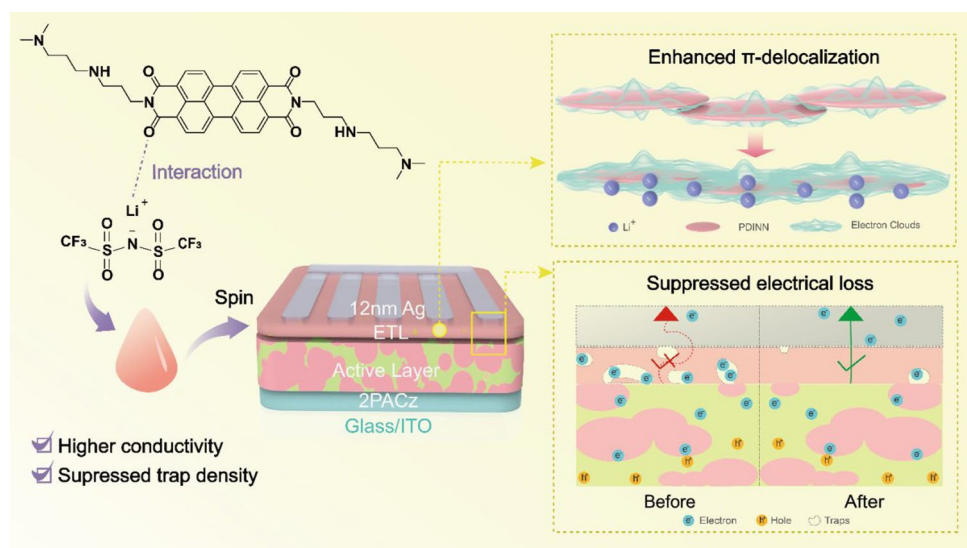
Scheme 1 Illustration of ETL doping process and electronic distribution evolution

2.2 Device Fabrication

STOPVs were fabricated with a conventional architecture of indium tin oxide (ITO)/PEDOT:PSS/active layer/ETL/Ag (12 nm). The ITO-coated glass substrates were pre-cleaned ultrasonically in water, acetone, and ethanol in sequence for 15 min and then treated with UV-ozone for 20 min. PEDOT:PSS 4083 was spin-coated at 3000 rpm for 30 s and annealed at 150 °C for 20 min. For better device performance, 2PACz was used to replace PEDOT:PSS 4083. 2PACz (0.3 mg mL^{-1} in ethanol) was spin-coated at 3000 rpm for 30 s and annealed at 100 °C for 5 min. PM6/BTP-eC9 (1:1.5, w/w) was dissolved in CB with a total concentration of 20 mg mL^{-1}, with 0.6 vol% DIO as addictive. The solution of PM6:BTP-eC9 needed to be stirred at 60 °C overnight until completely dissolved. The solution was spin-coated onto 2PACz or PEDOT:PSS 4083 modified substrate at 3200 rpm for 45 s to form active layer (80 nm). The active layer was then annealed at 100 °C for 5 min. A thin layer (~ 5 nm) of PDINN in methanol with a concentration of 1 mg mL^{-1} was spin-coated on the top of the active layer at 3000 rpm for 30 s. For PDINO-based STOPVs, PDINO was spin-coated at 3000 rpm for 30 s with a concentration of 1 mg mL^{-1} in methanol. For PNDIT-F3N-based STOPVs, ETL was spin-coated at 1500 rpm for 30s with a concentration of 1.5 mg mL^{-1} in methanol (0.5 vol% Acetic acid). Finally, 12 nm Ag was evaporated sequentially under high vacuum.

2.3 Device Characterization and Analysis

J–V characteristics were measured in the forward direction from − 0.5 to 1.5 V using computer-controlled Keysight B2901A Source Meter under the illumination of an Enlitech solar simulator (SS-X50, AAA grade) coupled with AM 1.5G solar spectrum filter in a nitrogen glove box at room temperature. The light intensity was calibrated to 100 mW cm^{-2} using a standard silicon reference cell (SRC2020). The devices were tested under a mask with an area of 2.56 mm^2. The EQE spectra were measured through the Solar Cell Spectral Response Measurement System QE-R (Enlitech Co., Ltd.). TPC and TPV were obtained by the all-in-one characterization platform, Paios (Fluxim AG, Switzerland). In TPC testing, the light intensities were 10%, 17.8%, 31.6%, 56.2%, and 100% sunlight, respectively. The settling time was 100 µs, pulse length was 100 µs, and the follow-up time was 200 µs. In the TPV testing, the light intensities were 0.10%, 0.21%, 0.44%, 0.93%, 1.95%, 4.10%, 8.62%, 18.11%, 38.06%, and 80.0% sunlight, respectively. The settling time was 30 ms, pulse length was 5 ms, and the follow-up time was 30 µs. The conductivity of ETLs was estimated by measuring the current–voltage (*I–V*) curves of the devices with the structure of ITO/ETL/Ag using Ohm's law (Fig. S1a). The pre-cleaned ITO substrates were treated with UV-ozone for 20 min. Then, the PDINN and D-PDINN were spin-coated on the ITO substrates. About

100 nm Ag was thermally evaporated under high vacuum. The $I–V$ characteristics of these devices were measured in the dark. The electron and hole mobility was measured by the SCLC method, the electron-only devices were fabricated with the structure of ITO/ZnO/active layer/ETL/Ag and the hole-only devices were fabricated with the structure of ITO/PEDOT:PSS/active layer/MoO$_3$/Ag. The mobility was calculated with the Mott–Gurney equation in the SCLC region:

$$J = \frac{9}{8}\varepsilon\varepsilon_0\mu\frac{V^2}{L^3}$$

where J is the current density, ε_0 is the permittivity of free space, ε_r is the relative permittivity of the material, L is the thickness of the active layer, and V is the effective voltage. The V_{TEF} of ETL was also measured by SCLC method, using the device structure of Au/ETL/Au. Methanol solutions of PDINN or D-PDINN were spin-coated at a film thickness of ~ 5 nm on substrates with parallel Au electrodes (thickness = 100 nm) (Fig. S1b).

3 Results and Discussion

3.1 Preparation and Characterization of LiTFSI Doped PDINN

The molecular structures of PDINN [42] and LiTFSI are shown in Fig. 1a. The molecular geometries of PDINN, LiTFSI, and their adduct were investigated using density functional theory with ORCA 5.0.4 [43, 44] and visualized with VMD [45]. According to the electrostatic potential distributions of PDINN and LiTFSI (Fig. S2), the carbonyl oxygen in PDINN is negatively charged and the Li$^+$ in LiTFSI is positively charged, allowing for a strong electrostatic attraction between them. Figure 1b shows the Fourier-transform infrared (FT-IR) spectra of PDINN and LiTFSI-doped PDINN (D-PDINN). The peak at 1651 cm^{-1} represents the stretching vibration of C=O bond in PDINN [42] which becomes boarder with the full width at half maximum
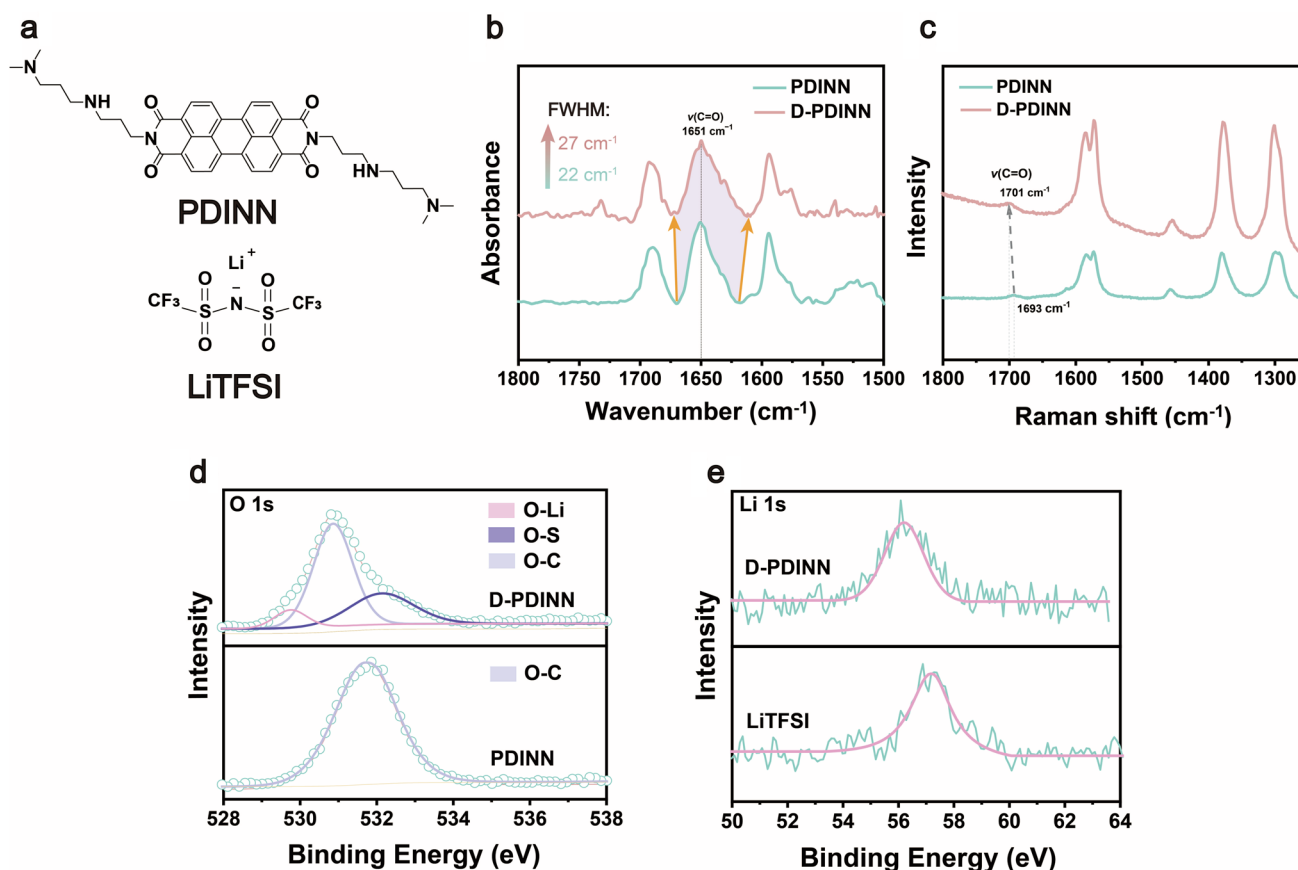

Fig. 1 Interaction between LiTFSI and PDINN. **a** Molecular structures of PDINN and LiTFSI. **b** FT-IR spectra of PDINN and D-PDINN. **c** Raman spectra of PDINN and D-PDINN. **d** O 1s XPS spectra of PDINN and D-PDINN. **e** Li 1s XPS spectra of LiTFSI and D-PDINN

(FWHM) increasing from 22 to 27 cm^{-1} after doping with LiTFSI, suggesting chemical environment around C=O has changed. Moreover, Raman spectra (Fig. 1c) show that the C=O peak blue-shifts from 1693 to 1701 cm^{-1} after the addition of LiTFSI, suggesting the electron density on C=O bond increases. X-ray photoelectron spectroscopy (XPS) was further employed to elucidate the interactions between PDINN and LiTFSI. The O 1s spectrum of PDINN shows a single peak at 531.7 eV (Fig. 1d), attributed to the binding energy of C–O binding [46]. As for D-PDINN, the O 1s peak can be decomposed into three peaks at 529.8, 530.9, and 532.1 eV, corresponding to Li–O, C–O, and S–O binding, respectively [47–49]. The binding energy shift of C–O peak indicates the chemical environment of carbonyl in PDINN changes after LiTFSI addition, suggesting carbonyl groups are the interaction sites in PDINN. The Li 1s XPS peak of LiTFSI locates at 57.2 eV (Fig. 1e), while that of D-PDINN shifts to 56.2 eV, implying Li$^+$ participates in the interaction [46, 47]. Collectively, these results suggest that PDINN and LiTFSI interact through interaction between carbonyl and Li$^+$.

To reveal the effects of LiTFSI doping, the π-electron delocalization of PDINN and D-PDINN was analyzed using localized orbital locator (LOL) with Multiwfn [50, 51]. At the same isovalue of 0.37, the LOL-π isosurface of PDINN is discontinued between the perylene and imide groups, while that of D-PDINN distributes across the perylene and an imide group, indicating the π electrons are more delocalized in D-PDINN (Fig. 2a). Electron paramagnetic resonance (EPR) spectroscopy is implemented to experimentally investigate the degree of electron delocalization. As shown in Fig. 2b, D-PDINN exhibits a stronger signal peak at the same position as PDINN with g factor of 2.004. Since the peak width is narrower than that of typical radicals, this peak is considered as a signal generated by the π electrons. The strengthened EPR signal in D-PDINN proves that LiTFSI induces more delocalized π electrons, which is beneficial to sizeable intermolecular π–π overlap and thereby enhanced the conductivity [52, 53]. Moreover, the π-delocalization is further investigated by ^{1}H NMR (Fig. 2c). After the doping with LiTFSI, the peaks representing aromatic protons shift upfield: the peak at δ 7.29 ppm shifts to δ 7.17 ppm, and that at δ 6.99 ppm shifts to δ 6.83 ppm. The upfield shift indicates higher electron density around the protons, which suggests an increased electron delocalization in the aromatic system.

The doping density (N_d) of PDINN and D-PDINN was measured with Schottky junction diodes and was calculated from the slope of the Mott–Schottky plot (Fig. 2d). The N_d of pure PDINN is 2.69×10^{16} cm^{-3}, and after LiTFSI doping, D-PDINN shows an increased N_d of 4.01×10^{16} cm^{-3}. For semiconductors, doping is one of the most effective strategies to increase charge carrier density and conductivity [53, 54]. I–V test was further conducted for ITO/PDINN or D-PDINN/Ag devices to determine the conductivity of the films (Fig. 2e). D-PDINN shows a higher conductivity of 1.71×10^{-4} S cm^{-1} than PDINN (9.67×10^{-5} S cm^{-1}), confirming that the enhanced π delocalization, coupled with higher doping density, is beneficial to the improved conductivity.

The addition of LiTFSI to PDINN effectively reduces the trap density of the film. According to the space charge limited current (SCLC) test under dark conditions (Fig. 2f) and capacitance measurements at different frequencies (Fig. S3), the trap-filled-limited voltage (V_{TFL}) and capacitance (C) of the D-PDINN are both lower than PDINN. According to the formula $N_{trap} = 2CV_{TFL}/qdA$ [55, 56] as the device area (A) and film thickness (d) remaining consistent between PDINN and D-PDINN, the lower V_{TFL} and C indicate that the trap density of the D-PDINN (7.26×10^{16} cm^{-3}) is well suppressed compared to PDINN (1.29×10^{17} cm^{-3}), which is beneficial to enhance charge extraction and suppress surface traps in STOPVs [57]. Additionally, atomic force microscopy was used to investigate the effects of LiTFSI on the morphology of PDINN (Fig. S4). The film surface becomes slightly smoother with root-mean-square roughness (R_q) decreasing from 0.930 to 0.774 nm after the addition of LiTFSI, which is beneficial to reduce contact resistance and leakage current. And as shown in Fig. S5, the almost identical scanning electron microscopy of PDINN/Ag (12 nm) and D-PDINN/Ag (12 nm) implies the doping strategy will have no effect the AVTs of STOPVs.

The average lateral conductivity of PDINN/Ag (12 nm) and D-PDINN/Ag (12 nm) was $(9.99 \pm 0.30) \times 10^4$ and $(1.16 \pm 0.03) \times 10^5$ S cm^{-1} (Fig. S6), respectively, suggesting ETL doping can improve the lateral conductivity of electrode. The energy level adjustment ability after LiTFSI doping is measured by ultraviolet photoelectron spectroscopy (UPS) and cyclic voltammetry tests. As shown in Fig. 2g D-PDINN can effectively reduce the work function (W_F) of the Ag/PDINN from 4.00 to 3.87 eV. The lower W_F implies a higher metal Fermi level,
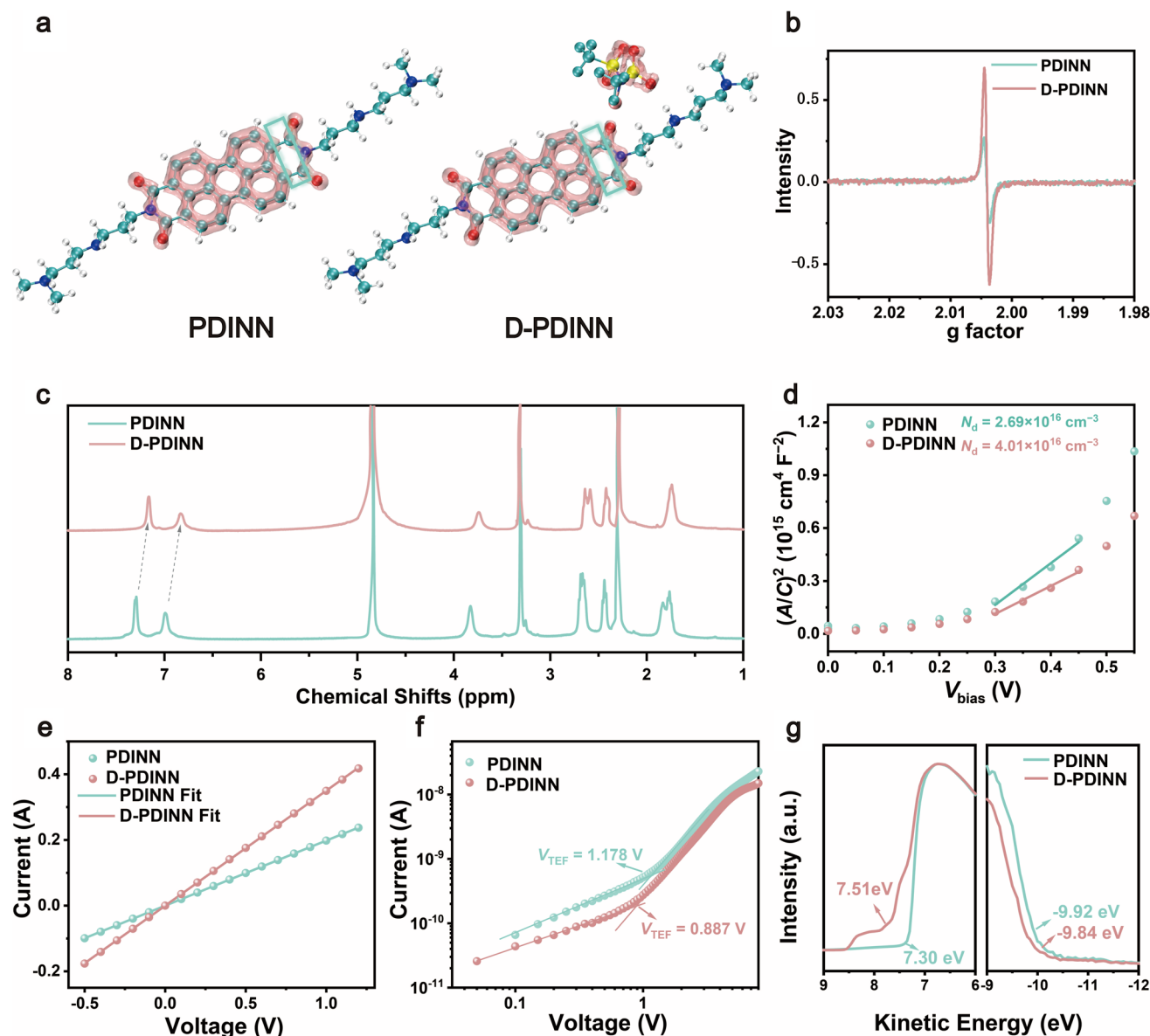
Fig. 2 Intrinsic performance of PDINN and D-PDINN. **a** LOL-π isosurface of PDINN and D-PDINN with isovalue of 0.37. **b** Electron paramagnetic resonance (EPR) spectrum of PDINN and D-PDINN. **c** ^{1}H HMR spectrum of PDINN and D-PDINN. **d** Mott–Schottky curves of ITO/PDINN or D-PDINN/Ag. **e** *I-V* curve for conductivity test. **f** SCLC curves of PDINN and D-PDINN with voltage increasing from 0 to 8 V. **g** UPS spectrum of Ag/PDINN and Ag/D-PDINN

which can form better ohmic contact between active layer and electrode to accelerate collection efficiency. Moreover, D-PDINN processes lower LUMO (− 3.87 eV) and HOMO (− 5.84 eV) energy levels compared to PDINN (Fig. S7), which is beneficial to electron extraction and hole blocking.

3.2 Photovoltaic Performance and Charge Carrier Dynamics

The structure of STOPV device is shown in Fig. 3a, and the molecular structures of used materials are shown in Fig. S8. The doping concentrations of LiTFSI in PDINN
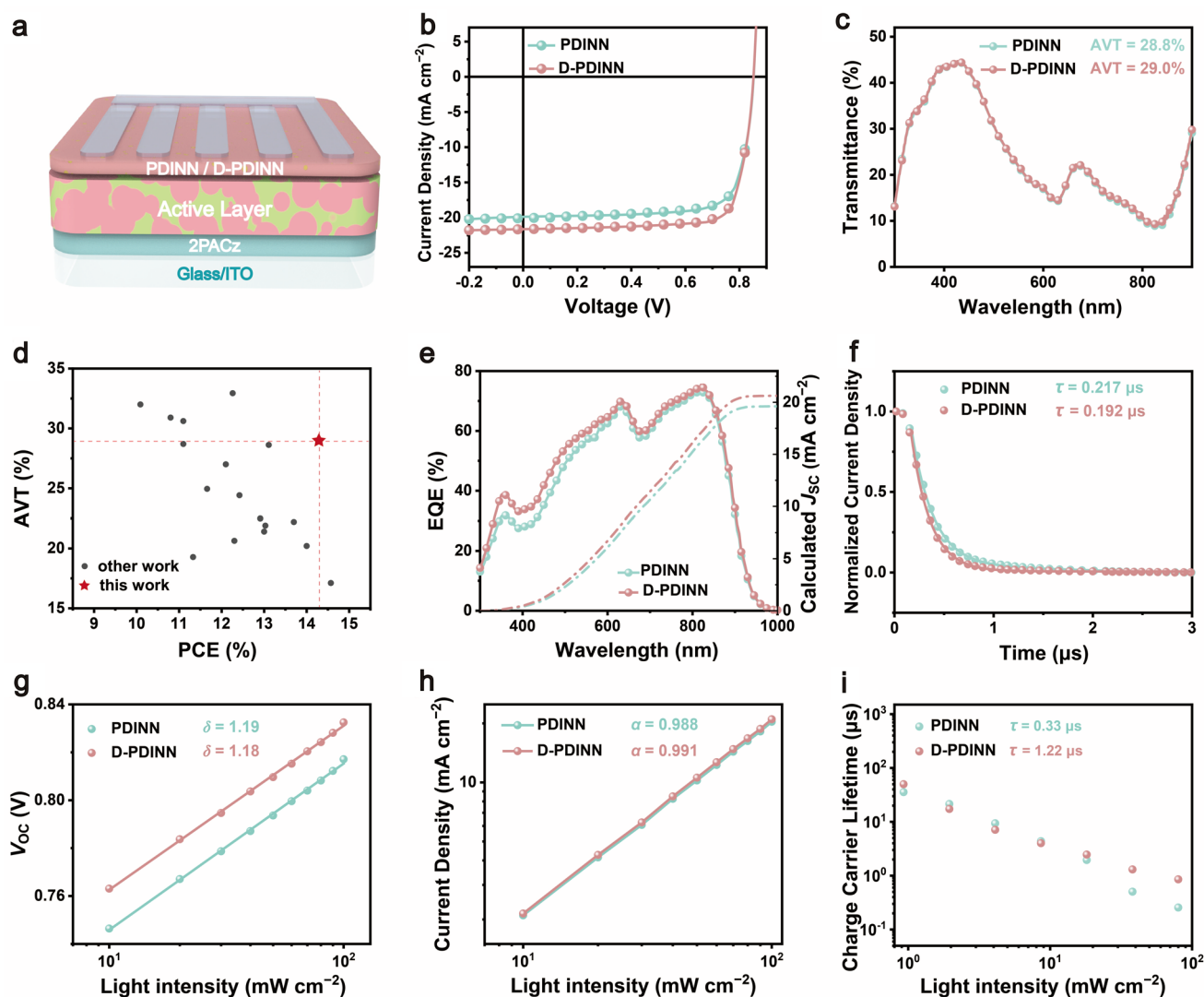
Fig. 3 Photoelectrical performance of PDINN- and D-PDINN-based STOPVs. **a** Structure of STOPV device. **b** Transmittance spectra of the PDINN- and D-PDINN-based STOPVs. **c** J–V curves of the PDINN- and D-PDINN-based STOPVs. **d** Comparison of PCE and AVT value among modulation-free STOPVs. **e** EQE spectra of the PDINN- and D-PDINN-based STOPVs. **f** Normalized TPC curves of the PDINN- and D-PDINN-based STOPVs. **g** Charge carrier lifetimes under different Plight obtained from TPV experiment of the PDINN- and D-PDINN-based STOPVs. **h** Dependence of V_{OC} on P_{light} and **i** dependence of J_{SC} on P_{light} of the corresponding STOPVs

were first optimized. As the molar ratio of LiTFSI/PDINN changing from 0.01% to 100%, the AVTs of STOPVs do not differ much (Fig. S9a), while the PCEs are substantially influenced (Fig. S9b). At the optimal LiTFSI/PDINN molar ratio of 1%, the STOPVs exhibit a champion PCE of 14.3%, with V_{OC}, J_{SC}, and FF of 0.846 V, 21.7 mA cm^{-2}, and 78.3%, respectively, higher than the PDINN-based control STOPVs with a PCE of 13.0%, V_{OC} of 0.845 V, J_{SC} of 20.0 mA cm^{-2}, and FF of 76.7% (Fig. 3b, Table 1). The AVT of PDINN- and D-PDINN-based devices is 28.8%

and 29.0% (Fig. 3c). Therefore, the LUE, of D-PDINN-based STOPVs is enhanced to 4.15%, which is among the highest values of optical structure-free STOPVs (Fig. 3d, Table S1). The external quantum efficiency (EQE) spectra of the PDINN- and optimal D-PDINN-based STOPVs are shown in Fig. 3e. D-PDINN-based STOPVs exhibit a higher EQE response from 300 to 1000 nm, which results in a higher integrated J_{SC} of 20.6 mA cm^{-2} compared to PDINN-based devices (19.6 mA cm^{-2}). The improvement of photovoltaic performance is also observed in opaque OPVs

Table 1 Device data of STOPVs with PDINN or optimal D-PDINN as ETLs

ETL	V_{OC} (V)	J_{SC} (mA cm^{-2})	FF (%)	PCE (%)[a]	cal. J_{SC} (mA cm^{-2})[b]	AVT (%)[c]	LUE (%)
PDINN	0.845 (0.845±0.001)	20.0 (20.3±0.2)	76.7 (75.0±0.9)	13.0 (12.9±0.1)	19.6	28.8	3.74
D-PDINN	0.846 (0.846±0.001)	21.7 (21.6±0.2)	78.3 (78.1±0.6)	14.3 (14.3±0.1)	20.6	29.0	4.15

[a] Averaged values with standard deviation in parentheses were obtained from 5 devices

[b] J_{SC} calculated from the integration of EQE spectra with the AM 1.5G spectrum

[c] Arithmetic mean of transmittance in 400–700 nm

with device structure of ITO/2PACz/PM6:BTP-eC9/PDINN or D-PDINN/Ag (120 nm). The PDINN-based OPVs yield a PCE of 18.7% with V_{OC} of 0.844 V, J_{SC} of 28.7 mA cm^{-2} and FF of 77.0%. By doping PDINN with LiTFSI, a higher J_{SC} of 29.2 mA cm^{-2} is achieved, along with higher slightly higher V_{OC} of 0.846 V and FF of 78.3%, leading to improved PCE of 19.4% (Table S2, Fig. S10a). The EQE spectra confirm that D-PDINN leads to a greater photon response from 300 to 1000 nm than OPVs based on PDINN (Fig. S10b).

Besides, the LiTFSI doping is also effective to STOPVs based on other carbonyl-rich ETLs. Table S3 summarizes the key photovoltaic parameters of the STOPVs based on PDINO and PNDIT-F3N (Fig. S11). As for PDINO-based control STOPVs, the AVT is 27.8% and PCE is 13.1% with J_{SC} of 20.5 mA cm^{-2}, V_{OC} of 0.833 V and FF of 76.6%. After doping PDINO with LiTFSI (D-PDINO), the AVT remains at 27.9%, while PCE improved to 13.7% with a higher J_{SC} of 21.3 mA cm^{-2}, leading to a higher LUE of 3.96% (Fig. S12a, b). When doping PNDIT-F3N with LiTFSI (D-PNDIT-F3N), the STOPVs yield a higher PCE of 14.9% with higher J_{SC} of 23.0 mA cm^{-2} than PNDIT-F3N based control STOPVs with PCE of 13.7% and J_{SC} of 21.6 mA cm^{-2} (Fig. S13a). The AVTs of PNDIT-F3N and D-PNDIT-F3N-based STOPVs are 23.4% and 23.7% (Fig. S13b). As shown in Figs. S12c and S13c, D-PDINO and D-PDNIT-F3N lead to greater response of STOPVs in EQE spectra, which is consist with the improved J_{SC}. The influence of doping strategy on PDINN- or D-PDINN-based STOPVs stability is investigated by storage under light (LED 100 mW cm^{-2}), in the N$_2$ atmosphere and ambient atmosphere (40% relative humidity), respectively. As shown in Fig. S14, the impact of LiTFSI doping strategy on the stability of STOPV devices is limited.

The effects of LiTFSI doping on charge extraction were investigated by transient photocurrent (TPC) test (Fig. 3f). The charge extraction time of D-PDINN-based STOPVs is

0.192 μs, shorter that of PDINN-based STOPVs (0.217 μs). The faster charge extraction in D-PDINN-based STOPVs benefits higher J_{SC} and FF, which can be attributed to the improved conductivity relative to pristine PDINN. Light intensity (P_{light}) dependence of V_{OC} and J_{SC} was used to characterize the charge recombination in the devices. The equation of $V_{OC} \propto (\delta kT/q) \ln (P_{light})$ describes the relationship between V_{OC} and P_{light}, where k, T, and q are the Boltzmann constant, temperature, and elementary charge, respectively. The δ represents whether the process is dominated by bimolecular recombination ($\delta \rightarrow 1$) or trap-assisted recombination ($\delta \rightarrow 2$). The δ values are calculated to be 1.19 for the PDINN-based STOPVs and 1.18 for the D-PDINN-based STOPVs (Fig. 3g), indicating that the trap-assisted recombination is slightly suppressed in D-PDINN-based devices. The J_{SC}–P_{light} dependence follows the relationship of $J_{SC} \propto P_{light}^{\alpha}$, where α represents the degree of bimolecular recombination and α closer to 1 means less bimolecular recombination. The D-PDINN-based STOPVs exhibit a higher α of 0.991 than PDINN-based counterparts (0.988) (Fig. 3h), indicating that bimolecular recombination is suppressed in the D-PDINN-based STOPVs. The weaker bimolecular recombination could be originated from the less charge carrier accumulation at the interface between active layer and ETL due to the enhanced conductivity of D-PDINN. The charge carrier lifetime (τ) in devices was extracted from transient photovoltage (TPV) experiments (Fig. 3i). The τ of D-PDINN-based devices is 1.22 μs, longer than that of 0.33 μs in PDINN-based ones, suggesting less charge recombination in D-PDINN-based STOPVs, consistent with the results from V_{OC}–P_{light} and J_{SC}–P_{light} analysis.

The light-to-electricity conversion processes in devices were evaluated by measuring the photocurrent density (J_{ph}) under different effective voltage (V_{eff}) (Fig. S15a). At high V_{eff} (> 2.90 V), all generated charges are swept out, and the J_{ph} becomes saturated photocurrent density (J_{sat}). The

J_{sat} of PDINN- and D-PDINN-based devices are 20.2 and 21.89 mA cm^{-2}, respectively. The ratio of J_{ph}/J_{sat} represents the overall efficiency of the light-to-electricity conversion at different V_{eff} (Fig. S15b). D-PDINN-based devices show higher J_{ph}/J_{sat} than PDINN-based devices, especially at low V_{eff} region. Since the active layers are the same, the exciton generation, charge separation, and charge transport can be assumed identical in these devices at a fixed V_{eff}. Therefore, the higher J_{sat} indicates more charges can be output due to the suppressed charge accumulation at the active layer/ETL interface and thereby less charge recombination during charge extraction process; and the higher J_{ph}/J_{sat} suggests the charge extraction in D-PDINN-based devices is more efficient, which is beneficial to higher V_{OC}, J_{SC}, and FF.

3.3 Quantitative Analysis for Recombination Current

The surface trap-assisted recombination is a major cause of the electrical loss in STOPVs [34], and the effects of LiTFSI doping on the traps and recombination current were investigated using capacitance spectroscopy [34, 58, 59]. To begin with, the capacitance of PDINN (Fig. 4a) and D-PDINN-based devices (Fig. 4b) was measured under the AM 1.5G irradiation at different biases and in the dark (Fig. S16a), from which the chemical capacitance (C_{chem}) (Fig. 4c) can be obtained to calculate the density of free charge carriers (n) (Fig. 4d) with V_{bi} from Mott–Schottky curves (Fig. S16b) and electron and hole mobility from SCLC tests (Fig. S17). The recombination current density (J_{rec}) is determined from J-V curves and can be fitted as the sum of bimolecular recombination current density ($J_{rec,bm}$), bulk trap-assisted recombination current density ($J_{rec,buk}$), and surface trap-assisted recombination current density ($J_{rec,surf}$), using bimolecular recombination coefficient (ξ), bulk trap density ($N_{t,bulk}$), and surface trap density ($N_{t,surf}$) as fitting parameters (Fig. 4e). The fitting details are presented in Supporting Information. PDINN-based devices show a ξ of 0.0127, $N_{t,\,bulk}$ of 2.22×10^{14} cm^{-3}, and $N_{t,\,surf}$ of 5.01×10^{10} cm^{-2}, while D-PDINN-based devices show a lower ξ of 0.0120,
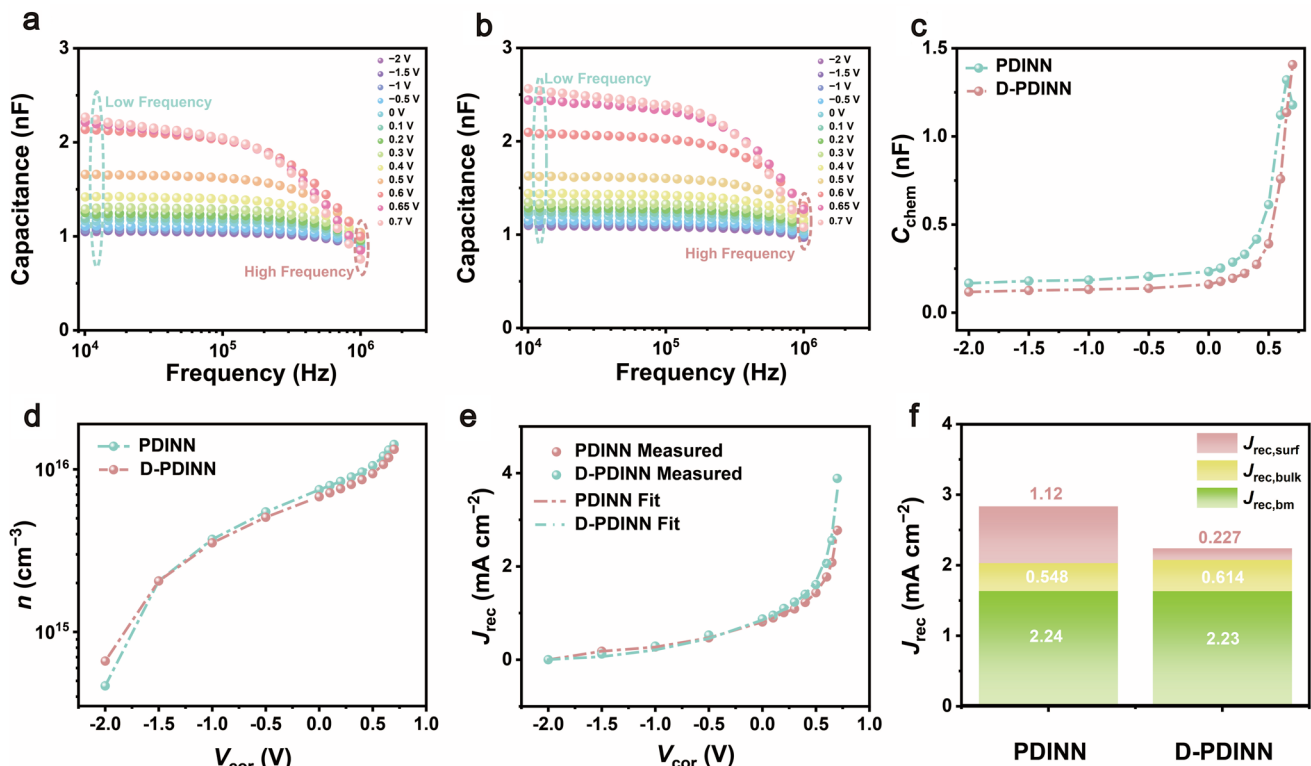

Fig. 4 Capacitance of **a** PDINN- and **b** D-PDINN-based STOPVs at different biases under the AM 1.5G illumination (100 mW cm^{-2}). **c** Chemical capacitance of the STOPVs based on PDINN and D-PDINN. **d** Charge carrier density of PDINN- and D-PDINN-based STOPVs. **e** Measured total recombination current densities and their fits for STOPVs based on PDINN and D-PDINN. **f** Histograms of recombination current densities for PDINN- and D-PDINN-based STOPVs

Table 2 Fitting parameters of the recombination current densities of PDINN- and D-PDINN-based STOPVs

ETL	ξ	$N_{t,\ bulk}$ (cm^{-3})	$N_{t,\ surf}$ (cm^{-2})
PDINN	0.0127	2.22×10^{14}	5.01×10^{10}
D-PDINN	0.0120	1.34×10^{14}	8.66×10^{9}

$N_{t,\ bulk}$ of 1.34×10^{14} cm^{-3}, and $N_{t,\ surf}$ of 8.66×10^{9} cm^{-2} (Table 2). The lower ξ suggests weaker bimolecular recombination, and lower $N_{t,\ bulk}$ and $N_{t,\ surf}$ correspond to suppressed trap-assisted recombination. Notably, D-PDINN-based STOPVs exhibit a 82.7% reduction in $N_{t,\ surf}$, which indicates the surface traps are effectively suppressed, contributing to lower photocurrent losses in STOPVs. Figure 4f shows the $J_{rec,\ bm}$, $J_{rec,\ buk}$, and $J_{rec,\ surf}$ in the STOPVs. In comparison with PDINN-based STOPVs, D-PDINN-based STOPVs showed slight suppression in $J_{rec,\ bm}$ and $J_{rec,\ buk}$. In contrast, the reduction in $J_{rec,\ surf}$ is more pronounced, reducing from 1.12 mA cm^{-2} in PDINN-based STOPVs to 0.227 mA cm^{-2} in D-PDINN-based ones. These results support the effectiveness of the LiTFSI doping strategy in inhibiting surface trap-assisted recombination, which is a primary cause of photocurrent loss in STOPVs, ultimately promoting the performance of STOPVs.

4 Conclusions

In summary, we present an effective strategy to enhance the charge collection ability and conductivity of the ultrathin Ag electrode in STOPVs via ETL doping. XPS and FT-IR results reveal that LiTFSI interacts with PDINN through the electrostatic attraction between Li$^+$ and carbonyl. Owing to this interaction, the π electrons in PDINN become more delocalized, as evidenced by the stronger EPR signal. As a result, relative to PDINN, D-PDINN shows increased conductivity from 9.67×10^{-5} to 1.71×10^{-4} S cm^{-1}, increased doping density from 2.69×10^{16} to 4.01×10^{16} cm^{-3}, and decreased trap density from 1.29×10^{17} to 7.26×10^{16} cm^{-3}. The W_F of D-PDINN decreases to 3.87 eV compared to 4.00 eV for PDINN/Ag, contributing to better ohmic contact between active layer and electrode. The optimized D-PDINN also provides lateral conductive channel for discontinuous ultrathin Ag electrode, improving its conductivity and charge collection ability. Consequently, D-PDINN-based STOPVs exhibit enhanced performance compared to PDINN-based

counterparts, with PCE increased from 13.0% to 14.3%, J_{SC} from 20.0 to 21.7 mA cm^{-2}, FF from 76.9% to 78.3%, and LUE from 3.74% to 4.15%. Charge dynamics in the devices were investigated by TPC, TPV, SCLC, light dependent test of J_{SC} and V_{OC} and capacitance spectroscopy, which demonstrates that D-PDINN-based STOPVs exhibit enhanced electron extraction, suppressed surface trap density and lower surface trap-assisted recombination current. This work provides a new mechanism of manipulating π-delocalization of ETL to optimize the electrical properties of ultrathin metal electrode and highlights the potential of interfacial engineering for efficient STOPVs. Based on this discovery, the future investigation can focus on exploring diverse cations with different valencies or ionic radii on and their influence on the properties of organic semiconductors.

Author Contribution Y.M., J.W., and P.C. conceived the idea and designed the experiments. Y.M. and J.L. fabricated the devices and Y.M. conducted related measurements. Y.M. and J.W. conducted the impedance measurements and recombination current density simulation. J.W. conducted the molecular simulation. H.C. conducted EPR measurements and analyzed the data. Y.G., L.M., and Y.L. conducted TPC and TPV measurements. J.Z. and L.F. fabricated and tested the ETL-only devices. C.Y. contributed to data analysis. Y.M. and J.W. wrote the paper. J.W. and P.C. supervised the project. All authors discussed the results and commented on the manuscript.

Declarations

References

1. S.-Y. Chang, P. Cheng, G. Li, Y. Yang, Transparent polymer photovoltaics for solar energy harvesting and beyond. Joule **2**(6), 1039–1054 (2018). https://doi.org/10.1016/j.joule.2018.04.005

2. Y. Hu, J. Wang, C. Yan, P. Cheng, The multifaceted potential applications of organic photovoltaics. Nat. Rev. Mater. **7**(11), 836–838 (2022). https://doi.org/10.1038/s41578-022-00497-y

3. V.V. Brus, J. Lee, B.R. Luginbuhl, S.-J. Ko, G.C. Bazan et al., Solution-processed semitransparent organic photovoltaics: from molecular design to device performance. Adv. Mater. **31**(30), e1900904 (2019). https://doi.org/10.1002/adma.201900904

4. H. Yu, J. Wang, Q. Zhou, J. Qin, Y. Wang et al., Semi-transparent organic photovoltaics. Chem. Soc. Rev. **52**(13), 4132–4148 (2023). https://doi.org/10.1039/d3cs00233k

5. T. Liu, M.M.S. Almutairi, J. Ma, A. Stewart, Z. Xing et al., Solution-processed thin film transparent photovoltaics: present challenges and future development. Nano-Micro Lett. **17**(1), 49 (2024). https://doi.org/10.1007/s40820-024-01547-6

6. E. Ravishankar, R.E. Booth, C. Saravitz, H. Sederoff, H.W. Ade et al., Achieving net zero energy greenhouses by integrating semitransparent organic solar cells. Joule **4**(2), 490–506 (2020). https://doi.org/10.1016/j.joule.2019.12.018

7. D. Wang, H. Liu, Y. Li, G. Zhou, L. Zhan et al., High-performance and eco-friendly semitransparent organic solar cells for greenhouse applications. Joule **5**(4), 945–957 (2021). https://doi.org/10.1016/j.joule.2021.02.010

8. N.C. Davy, M. Sezen-Edmonds, J. Gao, X. Lin, A. Liu et al., Pairing of near-ultraviolet solar cells with electrochromic windows for smart management of the solar spectrum. Nat. Energy **2**, 17104 (2017). https://doi.org/10.1038/nenergy.2017.104

9. D. Wang, Y. Li, G. Zhou, E. Gu, R. Xia et al., High-performance see-through power windows. Energy Environ. Sci. **15**(6), 2629–2637 (2022). https://doi.org/10.1039/d2ee00977c

10. N. Zhang, T. Jiang, C. Guo, L. Qiao, Q. Ji et al., High-performance semitransparent polymer solar cells floating on water: rational analysis of power generation, water evaporation and algal growth. Nano Energy **77**, 105111 (2020). https://doi.org/10.1016/j.nanoen.2020.105111

11. Z. Chen, J. Ge, W. Song, X. Tong, H. Liu et al., 20.2% efficiency organic photovoltaics employing a π-extension quinoxaline-based acceptor with ordered arrangement. Adv. Mater. **36**(33), 2406690 (2024). https://doi.org/10.1002/adma.202406690

12. Y. Sun, L. Wang, C. Guo, J. Xiao, C. Liu et al., π-extended nonfullerene acceptor for compressed molecular packing in organic solar cells to achieve over 20% efficiency. J. Am. Chem. Soc. **146**(17), 12011–12019 (2024). https://doi.org/10.1021/jacs.4c01503

13. J. Wang, P. Wang, T. Chen, W. Zhao, J. Wang et al., Isomerism effect of 3D dimeric acceptors for non-halogenated solvent-processed organic solar cells with 20% efficiency. Angew. Chem. Int. Ed. **64**(12), e202423562 (2025). https://doi.org/10.1002/anie.202423562

14. X. Li, X. Kong, G. Sun, Y. Li, Organic small molecule acceptor materials for organic solar cells. eScience **3**(5), 100171 (2023). https://doi.org/10.1016/j.esci.2023.100171

15. J. Wang, Y. Xie, K. Chen, H. Wu, J.M. Hodgkiss et al., Physical insights into non-fullerene organic photovoltaics. Nat. Rev. Phys. **6**(6), 365–381 (2024). https://doi.org/10.1038/s42254-024-00719-y

16. S. Guan, Y. Li, Z. Bi, Y. Lin, Y. Fu et al., Fine-tuning the hierarchical morphology of multi-component organic photovoltaics *via* a dual-additive strategy for 20.5% efficiency. Energy Environ. Sci. **18**(1), 313–321 (2025). https://doi.org/10.1039/d4ee03778b

17. N. Wei, J. Chen, Y. Cheng, Z. Bian, W. Liu et al., Constructing multiscale fibrous morphology to achieve 20% efficiency organic solar cells by mixing high and low molecular weight D18. Adv. Mater. **36**(41), 2408934 (2024). https://doi.org/10.1002/adma.202408934

18. H. Chen, Y. Huang, R. Zhang, H. Mou, J. Ding et al., Organic solar cells with 20.82% efficiency and high tolerance of active layer thickness through crystallization sequence manipulation. Nat. Mater. **24**(3), 444–453 (2025). https://doi.org/10.1038/s41563-024-02062-0

19. H. Li, Y. Li, X. Dai, X. Xu, Q. Peng, Ethanol processable inorganic-organic hybrid hole transporting layers enabled 20.12% efficiency organic solar cells. Angew. Chem. Int. Ed. **64**(4), e202416866 (2025). https://doi.org/10.1002/anie.202416866

20. Y. Wang, C. Gao, W. Lei, T. Yang, Z. Liang et al., Achieving 20% toluene-processed binary organic solar cells *via* secondary regulation of donor aggregation in sequential processing. Nano-Micro Lett. **17**(1), 206 (2025). https://doi.org/10.1007/s40820-025-01715-2

21. W. Kong, J. Wang, Y. Hu, N. Cui, C. Yan et al., P-type polymers in semitransparent organic photovoltaics. Angew. Chem. Int. Ed. **62**(45), e202307622 (2023). https://doi.org/10.1002/anie.202307622

22. X. Yan, J. Wang, W. He, T.A. Dela Peña, C. Zhu et al., Semitransparent organic photovoltaics enabled by transparent p-type inorganic semiconductor and near-infrared acceptor. J. Energy Chem. **96**, 351–358 (2024). https://doi.org/10.1016/j.jechem.2024.05.008

23. X. Huang, X. Ren, Y. Cheng, Y. Zhang, Z. Sun et al., Collaborative regulation strategy of donor and acceptor analogues realizes multifunctional semitransparent organic solar cells with excellent comprehensive performance. Energy Environ. Sci. **17**(8), 2825–2836 (2024). https://doi.org/10.1039/d3ee04476a

24. N. Gao, H. Bin, S. Wu, R.A.J. Janssen, Y. Li, Semitransparent organic solar cells with high light utilization efficiency and color rendering index. Sci. China Chem. **67**(7), 2248–2256 (2024). https://doi.org/10.1007/s11426-024-2056-9

25. J. Wang, J. Zhang, Y. Xiao, T. Xiao, R. Zhu et al., Effect of isomerization on high-performance nonfullerene electron acceptors. J. Am. Chem. Soc. **140**(29), 9140–9147 (2018). https://doi.org/10.1021/jacs.8b04027

26. C. Xu, K. Jin, Z. Xiao, Z. Zhao, X. Ma et al., Wide bandgap polymer with narrow photon harvesting in visible light range enables efficient semitransparent organic photovoltaics. Adv. Funct. Mater. **31**(52), 2107934 (2021). https://doi.org/10.1002/adfm.202107934

27. W. Liu, S. Sun, L. Zhou, Y. Cui, W. Zhang et al., Design of near-infrared nonfullerene acceptor with ultralow nonradiative voltage loss for high-performance semitransparent ternary organic solar cells. Angew. Chem. Int. Ed. **61**(19), e202116111 (2022). https://doi.org/10.1002/anie.202116111

28. D. Xie, Y. Zhang, X. Yuan, Y. Li, F. Huang et al., A 2.20 eV bandgap polymer donor for efficient colorful semitransparent organic solar cells. Adv. Funct. Mater. **33**(11), 2212601 (2023). https://doi.org/10.1002/adfm.202212601

29. J. Wang, P. Xue, Y. Jiang, Y. Huo, X. Zhan, The principles, design and applications of fused-ring electron acceptors. Nat. Rev. Chem. **6**(9), 614–634 (2022). https://doi.org/10.1038/s41570-022-00409-2

30. C. Xu, Z. Zhao, L. Kan, S. Tao, X. Ma et al., Colorful semitransparent organic photovoltaics with record key parameters by optimizing photon utilization and fabry-Pérot resonator electrode. Adv. Opt. Mater. **12**(10), 2302285 (2024). https://doi.org/10.1002/adom.202302285

31. L. Ma, S. Zhang, J. Zhu, Z. Chen, T. Zhang et al., Design of low-cost non-fused ultranarrow-band-gap acceptors for versatile photovoltaic applications. Joule **8**(8), 2238–2249 (2024). https://doi.org/10.1016/j.joule.2024.05.011

32. W. Xu, H. Zhou, H. Tian, L. Zhang, J. Du et al., Achieving light utilization efficiency of 3.88% and efficiency of 14.04% for semitransparent layer-by-layer organic solar cells by diluting donor layer. Chem. Eng. J. **508**, 161148 (2025). https://doi.org/10.1016/j.cej.2025.161148

33. H. Yu, J. Wang, Y. Li, T. Liu, Y. Gong et al., Mitigating interfacial recombination enabling efficient semitransparent organic photovoltaics. Chem. Eng. J. **499**, 156475 (2024). https://doi.org/10.1016/j.cej.2024.156475

34. Y. Li, J. Wang, C. Yan, S. Zhang, N. Cui et al., Optical and electrical losses in semitransparent organic photovoltaics. Joule **8**(2), 527–541 (2024). https://doi.org/10.1016/j.joule.2023.12.011

35. Y. Zhao, P. Cheng, H. Yang, M. Wang, D. Meng et al., Towards high-performance semitransparent organic

photovoltaics: dual-functional p-type soft interlayer. ACS Nano **16**(1), 1231–1238 (2022). https://doi.org/10.1021/acsnano.1c09018

36. Y. Li, C. He, L. Zuo, F. Zhao, L. Zhan et al., High-performance semi-transparent organic photovoltaic devices *via* improving absorbing selectivity. Adv. Energy Mater. **11**(11), 2003408 (2021). https://doi.org/10.1002/aenm.202003408

37. Y. Zhang, J. Zheng, Z. Jiang, X. He, J. Kim et al., Guided-growth ultrathin metal film enabled efficient semi-transparent organic solar cells. Adv. Energy Mater. **13**(7), 2203266 (2023). https://doi.org/10.1002/aenm.202203266

38. J.A. Venables, G.T. Spiller, M. Hanbucken, Nucleation and growth of thin films. Rep. Prog. Phys. **47**(4), 399–459 (1984). https://doi.org/10.1088/0034-4885/47/4/002

39. J. Yun, Ultrathin metal films for transparent electrodes of flexible optoelectronic devices. Adv. Funct. Mater. **27**(18), 1606641 (2017). https://doi.org/10.1002/adfm.201606641

40. J. Jing, S. Dong, K. Zhang, Z. Zhou, Q. Xue et al., Semitransparent organic solar cells with efficiency surpassing 15%. Adv. Energy Mater. **12**(20), 2200453 (2022). https://doi.org/10.1002/aenm.202200453

41. X. Duan, C. Liu, Y. Cai, L. Ye, J. Xue et al., Longitudinal through-hole architecture for efficient and thickness-insensitive semitransparent organic solar cells. Adv. Mater. **35**(32), 2302927 (2023). https://doi.org/10.1002/adma.202302927

42. J. Yao, B. Qiu, Z.-G. Zhang, L. Xue, R. Wang et al., Cathode engineering with perylene-diimide interlayer enabling over 17% efficiency single-junction organic solar cells. Nat. Commun. **11**(1), 2726 (2020). https://doi.org/10.1038/s41467-020-16509-w

43. F. Neese, The ORCA program system. WIREs Comput. Mol. Sci. **2**(1), 73–78 (2012). https://doi.org/10.1002/wcms.81

44. F. Neese, Software update: the ORCA program system: version 5.0. WIREs Comput. Mol. Sci. **12**(5), e1606 (2022). https://doi.org/10.1002/wcms.1606

45. W. Humphrey, A. Dalke, K. Schulten, VMD: visual molecular dynamics. J. Mol. Graph. **14**(1), 33–38 (1996). https://doi.org/10.1016/0263-7855(96)00018-5

46. W. Yu, Z. Yu, Y. Cui, Z. Bao, Degradation and speciation of Li salts during XPS analysis for battery research. ACS Energy Lett. **7**(10), 3270–3275 (2022). https://doi.org/10.1021/acsenergylett.2c01587

47. A. Etxebarria, S.L. Koch, O. Bondarchuk, S. Passerini, G. Teobaldi et al., Work function evolution in Li anode processing. Adv. Energy Mater. **10**(24), 2000520 (2020). https://doi.org/10.1002/aenm.202000520

48. S. Liu, J. Liu, G. Liu, Y. Liu, H. Zhong, Modulation of the morphology, surface energy and wettability of malachite through a S, O, O-ligand surfactant: mechanism and hydrophobization. Appl. Surf. Sci. **505**, 144467 (2020). https://doi.org/10.1016/j.apsusc.2019.144467

49. H. Jeong, R. Nandi, J.Y. Cho, P.S. Pawar, H.S. Lee et al., CZTSSe/Zn(O, S) heterojunction solar cells with 9.82% efficiency enabled via $(NH_4)_2S$ treatment of absorber layer.

Prog. Photovoltaics Res. Appl. **29**(10), 1057–1067 (2021). https://doi.org/10.1002/pip.3439

50. T. Lu, F. Chen, Multiwfn: a multifunctional wavefunction analyzer. J. Comput. Chem. **33**(5), 580–592 (2012). https://doi.org/10.1002/jcc.22885

51. T. Lu, Q. Chen, A simple method of identifying π orbitals for non-planar systems and a protocol of studying π electronic structure. Theor. Chem. Acc. **139**(2), 25 (2020). https://doi.org/10.1007/s00214-019-2541-z

52. X. Ding, J. Lv, Z. Liang, X. Sun, J. Zhao et al., Optimizing of cathode interface layers in organic solar cells using polyphenols: an effective approach. Adv. Energy Mater. **14**(36), 2401741 (2024). https://doi.org/10.1002/aenm.202401741

53. A.D. Scaccabarozzi, A. Basu, F. Aniés, J. Liu, O. Zapata-Arteaga et al., Doping approaches for organic semiconductors. Chem. Rev. **122**(4), 4420–4492 (2022). https://doi.org/10.1021/acs.chemrev.1c00581

54. I.E. Jacobs, A.J. Moulé, Controlling molecular doping in organic semiconductors. Adv. Mater. **29**(42), 1703063 (2017). https://doi.org/10.1002/adma.201703063

55. X. Zheng, S. Ahmed, Y. Zhang, G. Xu, J. Wang et al., Differentiating the 2D passivation from amorphous passivation in perovskite solar cells. Nano-Micro Lett. **18**(1), 62 (2025). https://doi.org/10.1007/s40820-025-01913-y

56. Z. Wan, R. Wei, Y. Wang, H. Zeng, H. Yin et al., Multifunctional MXene for thermal management in perovskite solar cells. Nano-Micro Lett. **18**(1), 18 (2025). https://doi.org/10.1007/s40820-025-01855-5

57. C. Zhu, Y. Wang, L. Meng, B. Qiu, J. Li et al., Bifunctional bridging capping layer enables 24.5% efficiency of perovskite solar cells with polymer-based hole transport materials. Sci. China Chem. **68**(1), 350–359 (2025). https://doi.org/10.1007/s11426-024-2142-4

58. V.V. Brus, C.M. Proctor, N.A. Ran, T.-Q. Nguyen, Capacitance spectroscopy for quantifying recombination losses in nonfullerene small-molecule bulk heterojunction solar cells. Adv. Energy Mater. **6**(11), 1502250 (2016). https://doi.org/10.1002/aenm.201502250

59. J. Vollbrecht, V.V. Brus, S.-J. Ko, J. Lee, A. Karki et al., Quantifying the nongeminate recombination dynamics in nonfullerene bulk heterojunction organic solar cells. Adv. Energy Mater. **9**(32), 1901438 (2019). https://doi.org/10.1002/aenm.201901438

Publisher's Note Springer Nature remains neutral with regard to jurisdictional claims in published maps and institutional affiliations.